Development of Novel and Ultra-High-Performance Supercapacitor Based on a Four Layered Unique Structure

Himanshu [1], S. Srinivasa Rao [2], Dinah Punnoose [1], P. Sathishkumar [1], Chandu V. V. Muralee Gopi [1], Naresh Bandari [1], Ikkurthi Kanaka Durga [1], T. N. V. Krishna [1] and Hee-Je Kim [1],*

[1] School of Electrical Engineering, Pusan National University, Busandaehak-ro 63beon-gil, Geumjeong-gu, Busan 46241, Korea; himanshuhimanshu820@gmail.com (H.); dinahpunnoose@gmail.com (D.P.); sathishnano2013@gmail.com (P.S.); naga5673@gmail.com (C.V.V.M.G.); naresh1.bandari@gmail.com (N.B.); Kanakadurga.ikkurthi@gmail.com (I.K.D.); vamsik.tirumalasetty@gmail.com (T.N.V.K.)
[2] Department of Mechatronics Engineering, Kyungsung University, 309 Suyeong-ro Nam-gu, Busan 48434, Korea; srinu.krs@gmail.com
* Correspondence: heeje@pusan.ac.kr; Tel.: +82-51-510-2364; Fax: +82-51-513-0212

check for updates

Abstract: This paper presents an electrode with a core/shell geometry and a unique four-layered porous wrinkled surface for pseudocapacitive supercapacitor applications. To design the electrode, Ni foam was used as a substrate, where the harmonious features of four constituents, ZnO (Z), NiS (N), PEDOT:PSS (P), and MnO_2 (M) improved the supercapacitor electrochemical performance by mitigating the drawbacks of each other component. Cyclic voltammetry and galvanostatic charge discharge measurements confirmed that the ZNPM hybrid electrode exhibited excellent capacitive properties in 2 M KOH compared to the ZNP, ZN, and solely Z electrodes. The ZNPM electrode showed superior electrochemical capacitive performance and improved electrical conductivity with a high specific capacitance of 2072.52 F g^{-1} at 5 mA, and a high energy density of 31 Wh kg^{-1} at a power density of 107 W kg^{-1}. Overall, ZNPM is a promising combination electrode material that can be used in supercapacitors and other electrochemical energy conversion/storage devices.

Keywords: cyclic voltammetry; galvanostatic charge-discharge; energy storage; core shell; hybrid structure

1. Introduction

Electrical energy storage is a priority focus of many researchers due to the increasing demand for renewable energy sources and reducing CO_2 emissions [1–6], as well as the increasing dependency on portable electronics, such as smart phones, iPads, laptops, and electrical vehicles, which require lithium-ion batteries [7–9]. Thus, supercapacitors (SCs) have attracted considerable attention over the last few decades because of their high-power density compared to batteries [10–16].

SCs need to have high energy storage capacity. Therefore, to construct SC electrodes, conducting polymers, carbon allotropes, and transition metal oxides/hydroxides are generally chosen because of their high theoretical specific capacitance [17–23]. On the other hand, the materials have their advantage and disadvantages. Current applications require a large energy density and high specific capacitance. To fulfil this requirement, the most promising action is to mix pseudocapacitive materials with highly conductive materials [24–28].

Various metal oxides and metal sulfides have pseudocapacitive properties [29–33]. Among the many metal oxide/hydroxide electrodes, RuO_2 is the most well-known pseudocapacitive material with a specific capacitance as high as 1300 F g^{-1} [34–36]. Albeit, it is expensive, cannot be used in

strong acidic electrolytes, and is not environmentally friendly. In contrast, other oxides, such as ZnO and MnO_2, are inexpensive, nontoxic, environmentally friendly, and can be used in array-supported core/shell electrodes to enhance the power, energy density, and electron and ion diffusion [37–42]. ZnO has attracted attention because of its wide direct band gap of 3.37 eV and huge exciton-binding energy of 6 meV. Its weak interfacial properties, however, limit its use in supercapacitor applications [43,44]. MnO_2 is the best alternative to RuO_2; however, MnO_2 electrodes have limitations, such as low electrical conductivity (between 10^{-5}–10^{-6} S/m) and poor rate performance [45]

To enhance the performance of MnO_2 electrodes, the major challenge is to improve the electrical conductivity. One way is to combine the MnO_2 material with conducting polymers, such as PEDOT:PSS [46,47]. This is an encouraging material for SC electrodes because of its high conductivity and good performance, even at high temperatures and humidity. PEDOT doped with PSS also shows improved flexibility. Chengjie Yin et al. published 83.7% capacitance retention at a high current density of 5 A g^{-1}; a high specific capacitance of 1234.5 F g^{-1} at a current density of 1 A g^{-1} by preparing an advanced supercapacitor hybrid electrode with deposit materials PEDOT-PSS/Ni-Mn-Co-O [48]. Previous papers suggested that the PEDOT-PSS polymers can perform rapid redox reactions on metal oxides and metal sulfides, such as NiS, CuS, CoS and FeS [49,50].

NiS has been studied extensively for use in many applications in SCs, such as hydrogen evolution and solar cells, because of its intriguing physical properties and different structure [51]. For example, R. Gao et al. fabricated NiS@CoS double-shelled supercapacitor electrode material [52]. Krishnamoorthy et al. deposited Ni_3S_2 on nickel foam using a solvent thermal synthesis method [53] Zhang et al. prepared Ni_3S_4@amorphous MoS_2 by a one-pot synthesis [54] The above mentioned published data confirmed that NiS electrodes are suitable for SCs because of their ease of fabrication, high surface area, low cost, high electronics conduction, and high electrochemical performance. On the other hand, the NiS structure deteriorates during the repeated ion diffusion process. Therefore, the NiS electrode alone is unsuitable for practical applications in pseudocapacitors.

One strategy for enhancing the overall performance of an electrode is the attractive combination of different materials. This paper presents a unique layered designed SC electrode to overcome the lack of conductivity, weak mechanical flexibility, low surface area, and capacitance loss during the cycling process, low power and energy densities, and electrolyte compatibility using a four material-based layered electrode in a KOH electrolyte with a Pt counter electrode and Ag/AgCl reference electrode. The electrode was prepared in such a way that a nickel foam substrate was coated sequentially with ZnO, NiS, PEDOT:PSS, and MnO_2. ZNPM showed enhanced electrochemical performance due to a combination of the unique properties of the components. The ZnO/MnO_2 core/shell nanostructure benefits the SC performance because the ZnO rooted core acts as a mechanical brace and successful electron transport chain, which amplifies the electro chemical process of MnO_2. The shell MnO_2 allows ion diffusion and energy storage capacity because of its nanoporous structure. Experiments conducted on the core/shell and binding materials, NiS/PEDOT:PSS (ZNPM), with a KOH electrolyte revealed them to be the best combination to improve the electrochemical performance of SCs.

2. Experimental Section

2.1. Chemicals

Zinc acetate dehydrate ($Zn(CH_3COOH)_2 \cdot 2H_2O$), ethanol, zinc nitrate hexahydrate ($Zn(NO_3)_2 \cdot 6H_2O$), hexamethylenetetramine (HMT) ($C_6H_{12}N_4$), Nickel(II) Chloride Hexahydrate ($NiCl_2 \cdot 6H_2O$), PEDOT:PSS, $KMnO_4$ were purchased from Sigma-Aldrich, Busan, South Korea.

2.2. Preparation of Z, ZN, ZNP and ZNPM Electrodes

A two-step chemical bath deposition method (CBD) was used to prepare ZnO NRs on Ni foam. First, as a precursor, a 10 mM zinc acetate dehydrate ($Zn(CH_3COOH)_2 \cdot 2H_2O$) solution was poured into ethanol and stirred for 30 min. The cleaned Ni foam was kept in the prepared solution at

90 °C for 1 h. After maturation of the seed layer, the samples were annealed at 65 °C in air for approximately 5 h. To grow the ZnO NRs, 0.015 M zinc nitrate hexahydrate ($Zn(NO_3)_2 \cdot 6H_2O$) and hexamethylenetetramine (HMT) ($C_6H_{12}N_4$) solutions were mixed at 95 °C for 15 h, and a seeded substrate was immersed into this aqueous solution. The samples were washed with deionized (DI) water and annealed at 65 °C for 5 h. The NF with the deposited ZnO NRs is the Z electrode.

To design the second electrode, NiS was deposited on the Z electrode, which is termed as the ZN electrode. To synthesize the NiS nanoparticles, the host precursor materials, such as 0.1 M Nickel(II) Chloride Hexahydrate ($NiCl_2 \cdot 6H_2O$) and 0.4 M thiourea, were dissolved in 40 mL of ethylene glycol. Subsequently, 0.2 M 3-MPA was added to the above mixture with stirring. The mixture was stirred for 60 min to complete the dissolution of the added chemicals. The mixture was then transferred to a Teflon lined autoclave and subjected to a hydrothermal treatment at 150 °C for 10 h. The autoclave was cooled naturally to room temperature and the as-obtained NiS material was filtered and washed two to three times with DI water and ethanol. The NiS was dried in a vacuum oven at 55 °C for 4 h. The resulting materials (NiS) were used to prepare the supercapacitor electrodes. To produce the ZN electrode, a second layer of NiS paste was applied to the Z electrode, which was then placed in a vacuum and dried for 4 h at 55 °C.

A third layer was coated on the ZN electrode to construct the ZNP electrode. ZN electrodes were immersed in a PEDOT:PSS solution for 10 min, which coated the ZN electrodes with polymer. Subsequently, the polymer coated electrode was kept in a vacuum for 12 h at 60 °C. MnO_2 is one of the most promising materials for supercapacitor practical applications. To utilize its pseudocapacitive properties, it was applied to the ZNP electrode. The ZNP was coated with MnO_2 nanoparticles. A 10 mM aqueous $KMnO_4$ solution was prepared and the ZNP electrodes were dipped in it. The electrodes were characterized using a variety of techniques. The specific capacitance and energy and power densities were calculated from the electrical measurements. ZNPM showed the highest specific capacitance of all of the electrode presented in this paper.

2.3. Characterization

The morphology was examined by scanning electron microscopy (SEM, Hitachi: SU-70, Tokyo, Japan) at an accelerating voltage of 5.0 kV and the elemental composition was analyzed by energy dispersive X-ray spectroscopy (EDX, KBSI, Busan, Korea). Transmission electron microscopy (TEM, Jeol Corporation, JEM 2011, Tokyo, Japan) images were recorded at the Busan KBSI centre at an accelerating 200 kV. The oxidation states of the elements in the four electrodes was examined by X-ray photoelectron spectroscopy (XPS, KBSI, Busan, Korea).

Cyclic voltammetry (CV) was conducted using a SP-150 Biologic science instrument three electrode cell; Ag/AgCl, Pt wire, and the four electrodes (Z, ZN, ZNP and ZNPM) were used as the reference, counter and working electrode, respectively, in a 2 M KOH electrolyte. The energy, power, and capacitance were calculated by galvanostatic charge-discharge (GCD) at different current densities. A Biologic potentiostat/galvanostat/EIS was used for electrochemical impedance spectroscopy (EIS, Paris, France).

3. Results and Discussion

3.1. Schematic Illustration

Firstly, ZnO NRs were prepared by facile CBD method. In the first step, ZnO seed layer was deposited on the Ni foam (Scheme 1a). Secondly, ZN electrode was fabricated by deposit NiS particles on the Z electrode (Scheme 1b). Thirdly, To coat the ZN electrode with polymer, the prepared electrode were dip-coated into PEDOT:PSS solution for 10 min. The polymer coated electrode was dried in a vacuum and resultantly a rough wrinkled surface (ZNP electrode, Scheme 1c). Lastly, a fourth layer of MnO_2 nanoparticle was applied on ZNP electrode by drop casted using 10 mM $KMnO_4$, which is termed as ZNPM (Scheme 1d).
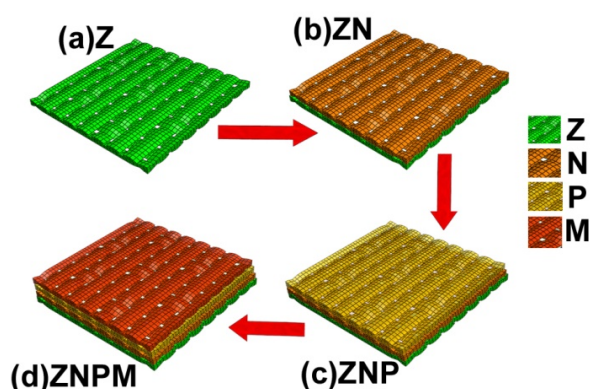
Scheme 1. Schematic illustration of presented layered supercapacitor electrodes (**a**) Z (**b**) ZN (**c**) ZNP (**d**) ZNPM.

3.2. Surface Morphology

Figure 1 presents SEM images and corresponding high magnifications images of electrodes Z, ZN, ZNP, and ZNPM. The extensive vertical growth of bare ZnO NRs (Figure 1a) distributed uniformly throughout the substrate was realized. Figure 1(a1) shows the morphology of the well-aligned ZnO NRs (Z) and the resulting cone-like morphology formed densely on the substrates. Higher magnifications revealed the hexagonal end surface of the NRs and their length and diameter were approximately 1 to 3 μm, respectively.

On the other hand, SEM showed that the surface of the NRs was rough after NiS (ZN) deposition. The rough texture of the nanoscale NiS coatings on these NRs were observed (Figure 1b, Figure 1(b1)). NiS was well crystallized with uniform nanospheres, 700 to 800 nm in diameter. NF is inactive in the KOH electrolyte and has a three-dimensional structure that contributes to the high specific surface area and escalates the adhesion of the NiS film. The strong adhesion plays a key role in thin film deposition, which affects the capacitance. The good adhesion of the material depends on the good wettability of the bonded surfaces by the liquid adhesive [55]. When PEDOT:PSS was deposited, the structure and surface adhesion was enhanced slightly. Figure 1c,d presents SEM images of ZNP and ZNPM films, respectively. Figure 1c shows a compact and rough morphology for the PEDOT:PSS film on ZN that exhibits a wrinkled surface morphology and a typical porous network structure Figure 1(c1). Figure 1d presents the ZNPM film, which shows that the material spreads out over the NF substrate. ZNPM and their corresponding high magnification images (a1, b1, c1 and d1).

TEM (Figure 2a) revealed ZnO NRs with a mean diameter of approximately 1–3 μm. The distribution of ZnO NRs is shown in the magnified image (Figure 2(a1)). When NiS was coated on ZnO, the TEM image of the prepared ZnO NRs revealed a smooth surface. The outer layers were composed of a solid Z core and shell. Figure 2c presents a representative TEM image of the obtained ZNP. The strong difference in contrast was observed in the nanoparticles from ZN to ZNP, where NRs were converted to distributed particles. These products were shorter than the ZnO NRs, indicating that they had broken into smaller sections during the chemical conversion process (Figure 2d).
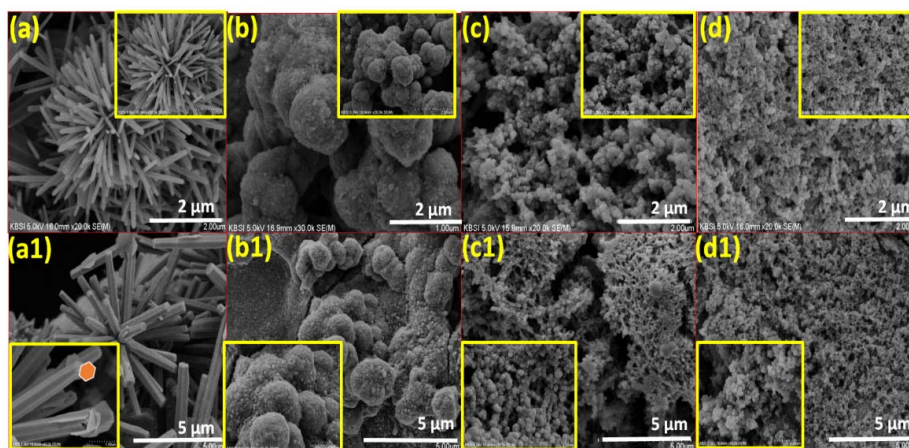
Figure 1. Field emission scanning electron microscopy images of (**a**) ZnO (**b**) ZnO/NiS (**c**) ZnO/NiS/PEDOT:PSS (**d**) ZnO/NiS/PEDOT:PSS/MnO$_2$ and their corresponding high magnification images (a1, b1, c1 and d1).
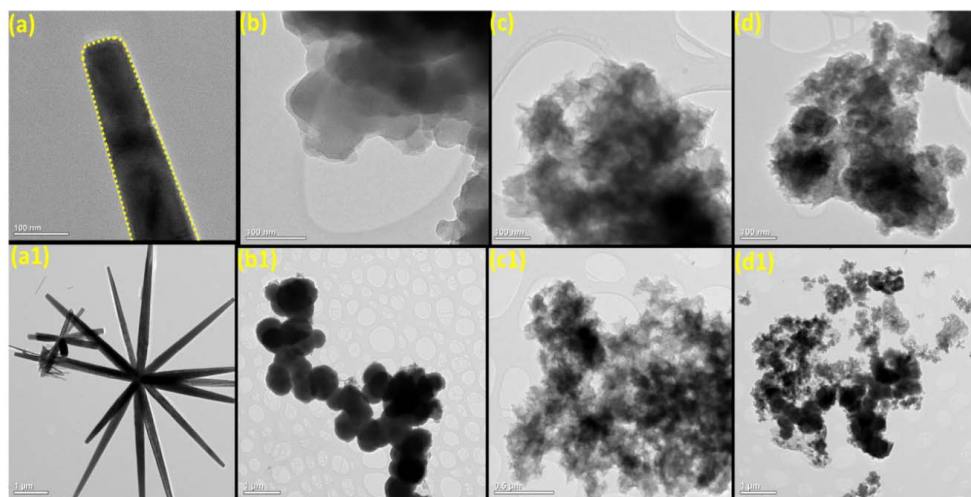
Figure 2. Transmission electron microscopy images of (**a**) Z (**b**) ZN (**c**) ZNP (**d**) ZNPM and the corresponding high magnification images (a1, b1, c1 and d1).

XPS was carried out for ZN and the results are shown in Figure 3a. The survey spectrum of ZN revealed S2p, C1s, O1s, Ni2p3, Zn2p3 and N1s at 162.89, 284.6, 531.14, 855.5, and 1072.12 eV, respectively. The O1s, C1s, and N1s peaks were attributed to exposure of the fabricated electrode to air. The binding energy of NiS at 853.2 and 870.5 eV corresponds to the presence of Ni2p3, and for the S2p spectrum of NiS. The binding energy at 161.4 eV suggests that S exists as S^{2-}, and the peaks for S2p$_{1/2}$ at 162.5 eV can be assigned to sulphur ions with low coordination at the NiS surface [56]. The peaks at 164.2 eV and 165.3 eV correspond to the sulfur atom of PEDOT and the higher binding energy peak at 168.5 eV corresponds to the sulfur atom present in PSS (Figure 3b) [57]. Figure 3c shows the survey spectrum of the ZNPM electrode, where the binding energy peaks at 642.48 eV for Mn 2p3 is shown along with Ni2p3 (855.16) and S2p (167.3). The survey spectrum was similar to those of ZN and ZNP, where the addition of Mn2p3 can be seen. The high resolution XPS scan of Mn 2p, showed two peaks at 642.48 and 653.32 eV, which were assigned to Mn 2p$_{3/2}$ and Mn 2p$_{1/2}$ respectively, and were separated by 10.84 eV.

Figure 4a–d presents the energy dispersive spectra and element maps of Z, ZN, ZNP, and ZNPM, respectively. SEM (Figure 4a–c) revealed a change in structure from nanorods to a flowery wrinkled

porous surface. The combination of new materials changed the morphology of the structure. Figure 4a shows the Z electrode containing 81.53% Zn and 34.49% O. In contrast, with the fourth electrode, ZNPM, typical peaks of Zn (0.23%), O (23.86%), Ni (27.32%), S (5.72%), Pd (0.58%), Mn (23.65%), and K (10.15%) were observed, as shown in Figure 4d. XPS and EDX showed that the Z, Zn, ZNP, and ZNPM were deposited successfully on the Ni foam substrate.
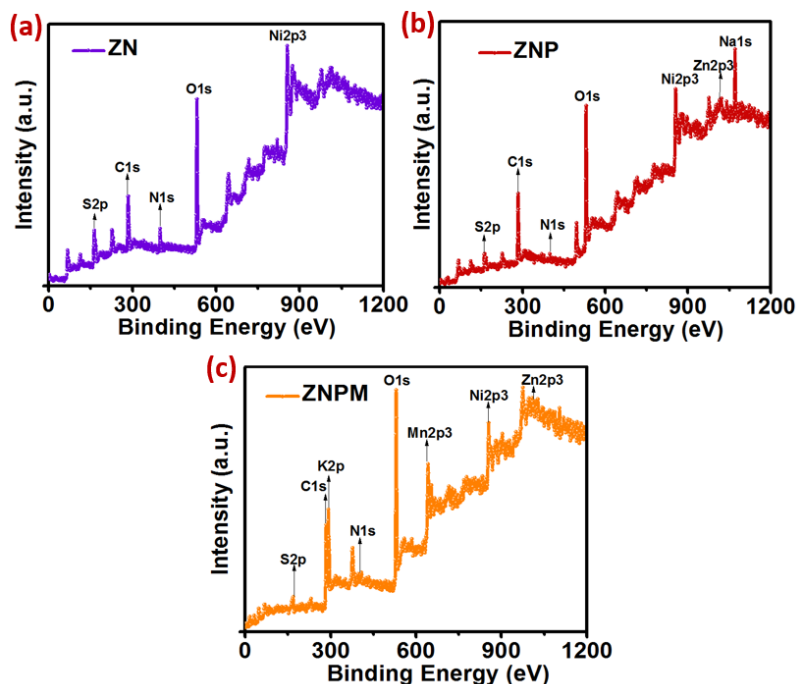

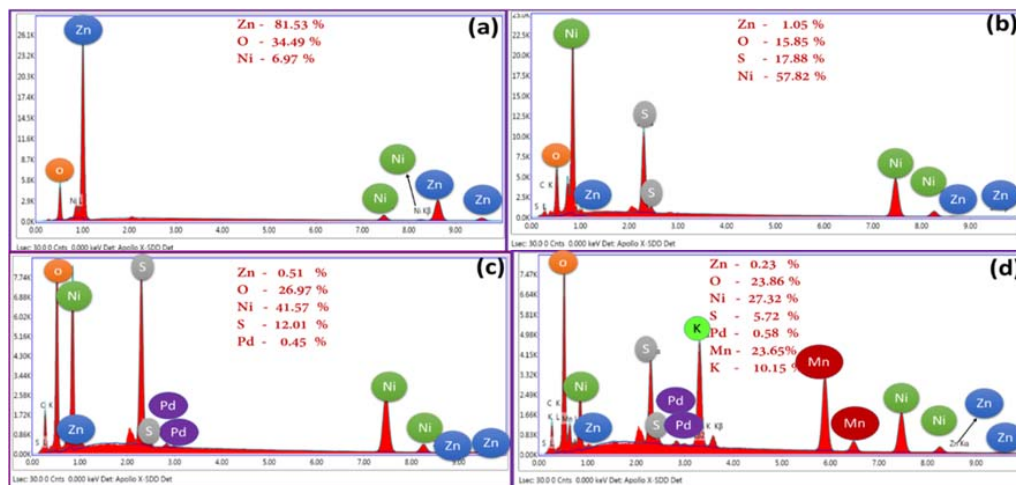**Figure 3.** XPS survey spectrum of (**a**) ZN (**b**) ZNP and (**c**) ZNPM.

Figure 4. EDX analysis of (**a**) Z, (**b**) ZN, (**c**) ZNP and (**d**) ZNPM.

3.3. Electrochemical Studies

The electrochemical capacitive performance of the bare ZnO and hybrid structures, ZN, ZNP, and ZNPM, were evaluated by CV and GCD techniques. Figure 5a–d shows the CV curves of ZN, ZNP, and ZNPM, respectively. The CV curves were obtained in a 2 M KOH aqueous solution. All the electrodes delivered a pair of redox peaks, indicating that all electrodes exhibit Faradic pseudo capacitance behaviour. Furthermore, due to polarization of the electroactive materials, the anodic and

cathodic peaks were slightly shifted towards higher and lower potentials under the increased scan rates. The ZNPM curves showed a rectangular and symmetric shape indicating a rapid and reversible redox reaction similar to that of an ideal supercapacitor. ZNPM showed the best performance compare to other three electrodes. This is because the ZNPM electrode-coated material provides a large active surface area, which allows smoother electron flow and shows the largest redox peak current density, which has oxidation and reduction currents are 121.98 mA and −86.33 mA, respectively. The enclosed area in the CV curve was highest with the ZNPM electrode, indicating that ZNPM has superior capacitance to the other three electrodes.
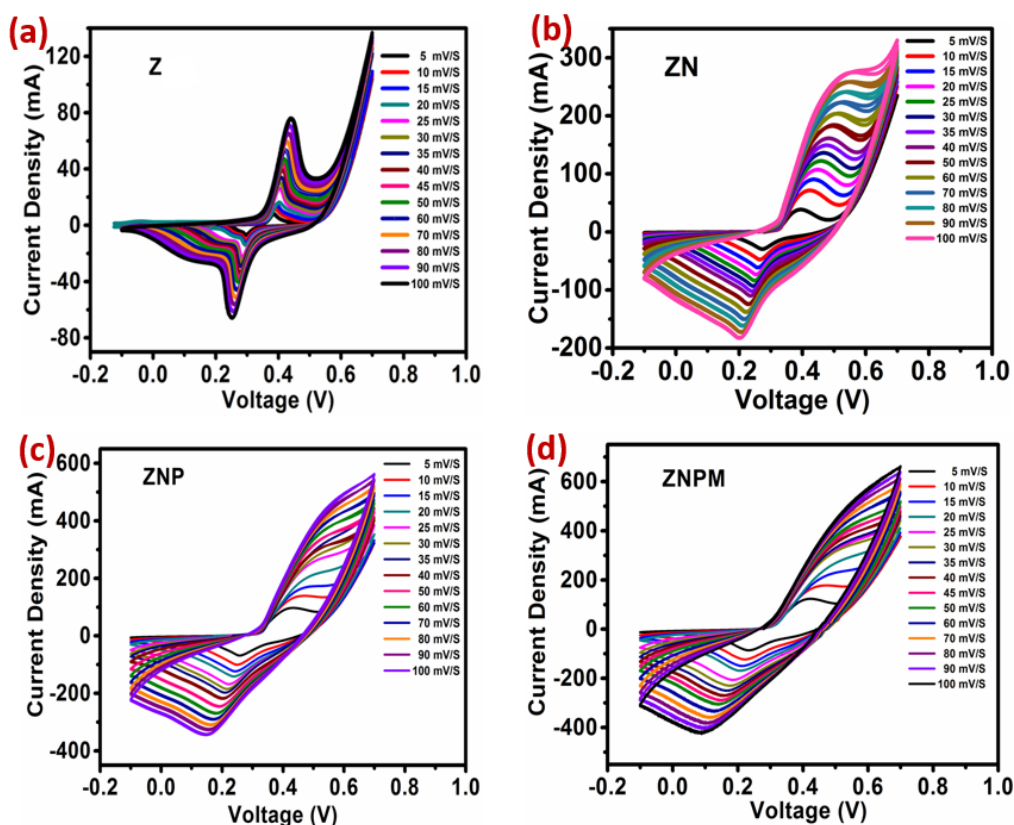

Figure 5. CV of (**a**) Z (**b**) ZN (**c**) ZNP and (**d**) ZNPM at different scan rates in a 2 M KOH solution.

Two main factors for the practical use of supercapacitors are the specific capacitance and energy density. GCD experiments were carried out on the Z, ZN, ZNP, and ZNPM electrodes to examine the specific capacitance and energy density in the potential range of −1 to 0.4 V at different current densities. The results are shown in Figure 6a–d, respectively. We have performed GCD analysis for bare nickel foam and observed very low specific capacitance which is negligible (Figure S1). The non-linear variation of the potential versus charge/discharge time clearly shows that the discharge time of the ZNPM electrode was significantly higher than that of the other three electrodes, including the visible enhanced symmetrical profiles at the ZNPM electrodes, indicating an increase in the conductivity in the core supporting nanowires. The specific capacitance can be calculated from the following Equation (1):

$$Cs = \frac{i\Delta t}{m\Delta V} \tag{1}$$

where *Cs* is the specific capacitance (F/g); *i* is the discharge current (A); Δt is the discharge time (*s*); ΔV is the potential window (V); and m is the mass of the electrode active material. The *Cs* values were calculated from the discharge curves in Figure 6a–d and the result is plotted in Table 1. Table 1 lists the specific capacitance of the electrodes at current densities of 5–100 mA. The increase in current density

was attributed to the decrease in specific capacitance. This is because of the diffusion effect of OH^- ions within the electrode at high current densities.
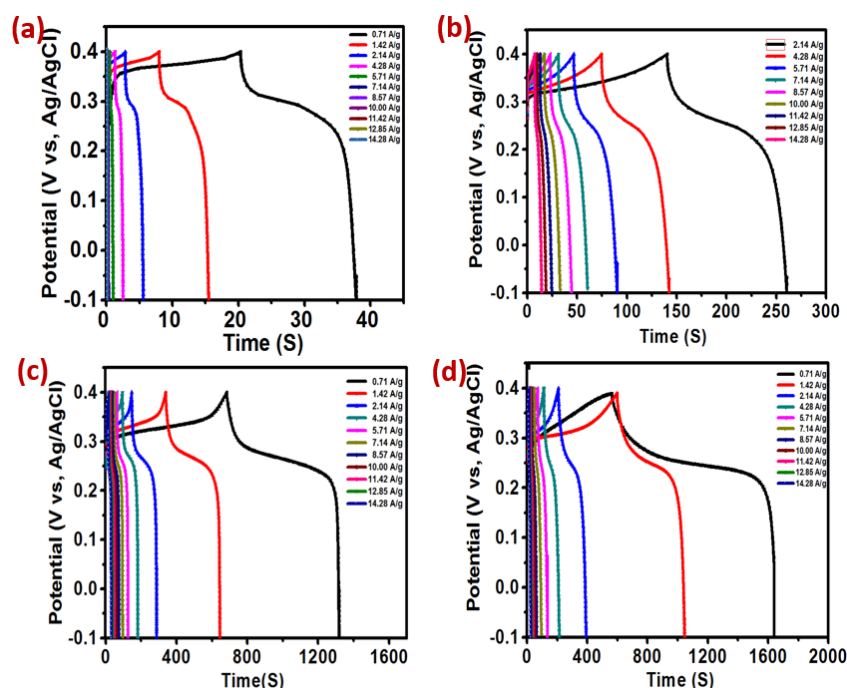

Figure 6. GCD curves of (**a**) Z (**b**) ZN (**c**) ZNP and (**d**) ZNPM at different current densities.

A comparison of the GCD curves of Z, ZN, ZNP and ZNPM electrodes at 5 mA were shown in Figure S2. At a low current density of 5 mA, the specific capacitance of Z, ZN, ZNP and ZNPM were approximately 24.77, 919.44, 1716.08, and 2072.52 F g^{-1}, respectively. A specific capacitance of four-layer electrodes exhibited higher showing improved performance for the four layer electrode compare to the three, two and bare ZnO nanowires. The ZN electrode showed higher specific capacitance due to the NiS porous structure. Remarkably, specific capacitance of ZNPM (2072.52 F g^{-1} at 0.71 A g^{-1}) is superior to previously reported WO_3@CuO (284 F g^{-1} at 1 A g^{-1}) [58], N-MWCNT/Co_3O_4 (406 F g^{-1} at 2 A g^{-1}) [59], ZnO/activated carbon (155 F g^{-1} at 0.5 A g^{-1}) [60], ZnO/C (820 F g^{-1} at 1 A g^{-1}) [61], G-ZnO (122.4 F g^{-1} at 2.13 A g^{-1}) [62]. On the other hand, the ZNP electrode surface morphology was updated by the wrinkled and porous network structure. This assists the electrolyte ion permeability, leading to a rapid redox reaction between the electrode and electrolyte. ZNP and ZNPM showed similar surface morphologies, so that almost identical diffusion was expected. The presence of MnO2 results in a high energy density and large charge transfer-reaction. The poor conductivity of MnO_2 was overcome by combining it with highly conductive PEDOT:PSS. Therefore, the increased electrochemical performance could be attributed to the development of conductivity in the core–supporting nanowire material. The relatively high specific capacitance of the ZNPM hierarchical architecture can be attributed to the four materials combining the characteristic unique structures, providing rapid ion and electron transfer.

EIS plots (Figure 7) of Z and ZNPM electrodes provided more information on their electrochemical performance. The Nyquist plot includes a partial semicircle in the high-frequency region indicates the charge transfer resistance (R_{ct}) and a straight line at the low-frequency region represents the repaid ion/electron transportation. The equivalent series resistance (R_S) can be calculated from the intercepts of the high-frequency semicircle on the real axis. The R_S (0.39 Ω) and R_{ct} (0.62 Ω) of Z were higher compared with ZNPM based electrode (R_S = 0.30 Ω and R_{ct} = 0.50 Ω). The low values of R_S and R_{ct} convey that all four layers of the material on the Ni substrate stick very well together

and have excellent electrochemical conductivity, rapid electron transfer kinetics, and diffusion of ions at the interface of electrode/electrolyte. In addition, the slope of the plot at low frequency for ZNPM electrode was steeper than Z electrode, revealing faster kinetics of the ions diffusion process. The ZNPM electrode-based supercapacitor performance was improved considerably compared to the Z electrode. One of the reasons is the equivalent series resistance for ZNPM, which was much lower than Z.

Table 1. Specific capacitance values of Z, ZN, ZNP, and ZNPM at different current densities.

Current Densities (mA)	Z (F g^{-1})	ZN (F g^{-1})	ZNP (F g^{-1})	ZNPM (F g^{-1})
5	24.77	919.44	1716.08	2072.52
10	20.68	871.71	1700.57	1900.57
20	13.02	779.37	1519.02	1697.02
30	10.40	765.08	1239.6	1459.31
40	5.37	735.54	1134.17	1205.22
50	2.15	667.42	1034.14	1152.04
60	1.23	632.22	939.94	1064.5
70	0.7	596.4	850.4	940.21
80	0.57	537.82	806.62	987.74
90	0.51	480.34	680.14	813.65
100	0.45	450.57	620.57	851.32
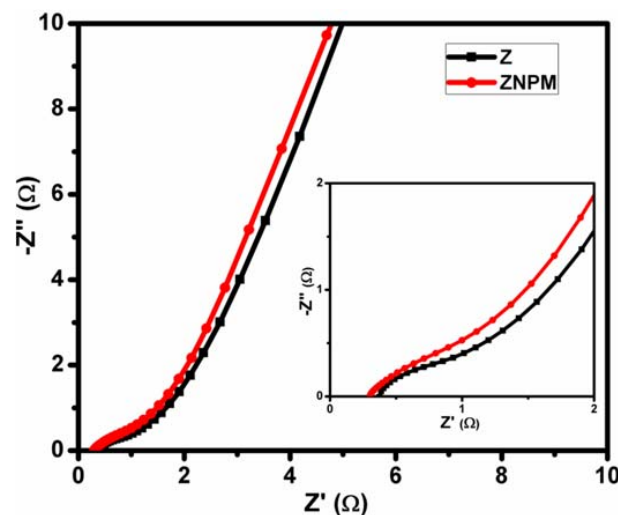
Figure 7. Electrochemical impedance spectroscopy of Z and ZNPM electrodes on nickel foam substrate. Inset shows the high magnified impedance plot.

The energy-power performance delivered by the ZNPM was much higher than that of the Z electrode, as shown in Figure 8. This was attributed to the densities through the charge and discharge curves at different current densities evaluated using the following Equations (2) and (3):

$$E = \frac{1}{2Cs(\Delta V)^2} \times \frac{1000}{3600} \tag{2}$$

$$P = \frac{E}{t} = \frac{i\Delta V}{2m} \times 1000 \tag{3}$$

P (kW/kg), *E* (Wh/kg) and *t*(s) are the power density, energy density, and discharge time, respectively. Based on above data, even at a high-power density of ~2142 W/kg, the ZNPM electrode showed an energy density of ~6.9 Wh/kg while the Z electrode was only ~0.041 Wh/kg. On the other hand, at low power density, ~150 W/kg, the energy density for ZNPM and Z was ~13 Wh/kg

and ~ 0.83 Wh/kg, respectively. The energy density decreased to ~12.17 Wh/kg. The energy-power performance of ZNPM was higher than that of Z due to the higher specific capacitance registered at ZNPM. The cycling stability of the prepared ZNP and ZNPM electrodes was additional inspected by GCD tests at a current density of 5 mA for 3000 cycles. As shown in Figure S3b, the specific capacitance of the ZNPM based electrode remains to be 1954.38 F g^{-1} after 3000 cycles with a retention of 94.3% of the initial specific capacitance (2072.52 F g^{-1}), which is higher compared to ZNP electrode (86.1% retention). Indicating that the charge/discharge process for the ZNPM electrode is substantially reversible, the materials architecture and the pore accessibility for electrolyte ions are highly stable upon long-term cycling tests. Moreover, we have included field emission scanning electron microscopy images for the ZNPM after 3000 cycles in KOH solution (Figure S4). Still we can see many nanoparticles spread on nickel foam substrate which shows that the ZNPM electrode is effective for supercapacitor application.
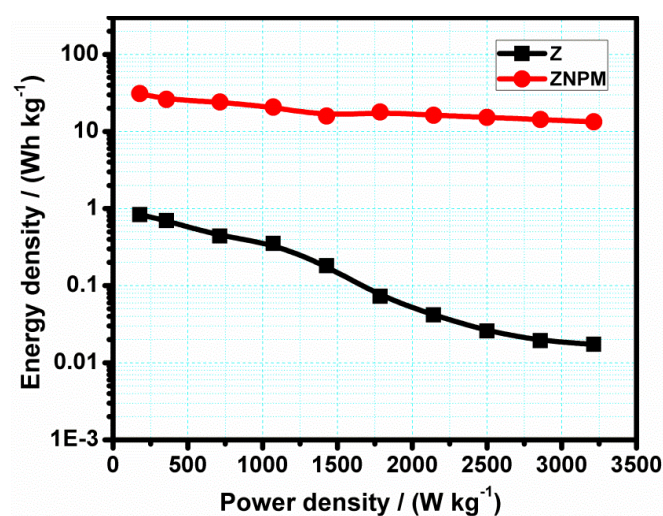

Figure 8. Power density vs. energy density of the Z and ZNPM hybrid electrodes.

4. Conclusions

ZnO NRs were used as a base for fabricating four pivotal components; ZNPM, for hybrid core/shell structure electrodes in supercapacitor applications. Each layer of a new component on the electrode increased the specific capacitance compared to the single component layer. The measured specific capacitance of Z, ZN, ZNP, and ZNPM was 24.77 F g^{-1}, 919.44 F g^{-1}, 1716.08 F g^{-1}, and 2072.52 F g^{-1}, respectively.

The interconnected arrangements of four layered unique structure of ZNPM electrode resulted in less resistance to ion transportation, large surface area, super electronic conductivity, as well as improved cycling stability, rate capability, and high energy and power densities. Overall, the ZNPM electrodes exhibited better electrochemical performance than the other electrodes. This technique of producing electrode materials will allow the fabrication of more promising electrode materials for future supercapacitor applications.

References

1. Ntona, E.; Arabatzis, G.; Kyriakopoulos, G.L. Energy saving: Views and attitudes of students in secondary education. *Renew. Sustain. Energy Rev.* **2015**, *46*, 1–15. [CrossRef]
2. Kyriakopoulos, G.L.; Arabatzis, G. Electrical energy storage systems in electricity generation: Energy policies, innovative technologies, and regulatory regimes. *Renew. Sustain. Energy Rev.* **2016**, *56*, 1044–1067. [CrossRef]
3. Guney, M.S.; Tepe, Y. Classification and assessment of energy storage systems. *Renew. Sustain. Energy Rev.* **2017**, *75*, 1187–1197. [CrossRef]
4. Muruganantham, B.; Gnanadass, R.; Padhy, N.P. Challenges with renewable energy sources and storage in practical distribution systems. *Renew. Sustain. Energy Rev.* **2017**, *73*, 125–134. [CrossRef]
5. Qiao, J.; Liu, Y.; Hong, F.; Zhang, J. A review of catalysts for the electroreduction of carbon dioxide to produce low-carbon fuels. *Chem. Soc. Rev.* **2014**, *43*, 631–675. [CrossRef] [PubMed]
6. Zhao, G.; Huang, X.; Wang, X.; Wang, X. Progress in catalyst exploration for heterogeneous CO_2 reduction and utilization: A critical review. *J. Mater. Chem. A* **2017**, *5*, 21625–21649. [CrossRef]
7. Taberna, P.L.; Mitra, S.; Poizot, P.; Simon, P.; Tarascon, J.-M. High rate capabilities Fe_3O_4-based Cu nano-architectured electrodes for lithium-ion battery applications. *Nat. Mater.* **2006**, *5*, 567–573. [CrossRef] [PubMed]
8. Howard, W.G.; Schmidt, C.L.; Scott, E.R. Lithium-Ion Battery 2010. U.S. Patent 7794869B2, 14 September 2010.
9. Scott, E.R.; Howard, W.G.; Schmidt, C.L. Lithium-Ion Battery 2010. U.S. Patent 7811705B2, 12 October 2010.
10. Aneke, M.; Wang, M. Energy storage technologies and real life applications—A state of the art review. *Appl. Energy* **2016**, *179*, 350–377. [CrossRef]
11. Gallo, A.B.; Simões-Moreira, J.R.; Costa, H.K.M.; Santos, M.M.; Moutinho dos Santos, E. Energy storage in the energy transition context: A technology review. *Renew. Sustain. Energy Rev.* **2016**, *65*, 800–822. [CrossRef]
12. Winter, M.; Brodd, R.J. What Are Batteries, Fuel Cells, and Supercapacitors? (*Chem. Rev.* **2003**, *104*, 4245−4269. Published on the Web 09/28/2004.). *Chem. Rev.* **2005**, *105*, 1021. [CrossRef]
13. Goodenough, J.B.; Lee, H.Y.; Manivannan, V. Supercapacitors and Batteries. MRS Online Proceedings Library Archive. Available online: https://www.cambridge.org/core/journals/mrs-online-proceedings-library-archive/article/supercapacitors-and-batteries/2C5873B0CEB69250059AD6BE41D5703E1998 (accessed on 15 February 2011).
14. Xia, X.; Chao, D.; Ng, C.F.; Lin, J.; Fan, Z.; Zhang, H.; Shen, Z.X.; Fan, H.J. VO_2 nanoflake arrays for supercapacitor and Li-ion battery electrodes: Performance enhancement by hydrogen molybdenum bronze as an efficient shell material. *Mater. Horiz.* **2015**, *2*, 237–244. [CrossRef]
15. Hadjipaschalis, I.; Poullikkas, A.; Efthimiou, V. Overview of current and future energy storage technologies for electric power applications. *Renew. Sustain. Energy Rev.* **2009**, *13*, 1513–1522. [CrossRef]
16. Xue, X.D.; Raman, S.R.; Fong, Y.C.; Cheng, K.W.E. Loss analysis of hybrid battery-supercapacitor energy storage system in EVs. In Proceedings of the 2017 7th International Conference on Power Electronics Systems and Applications—Smart Mobility, Power Transfer Security (PESA), Hong Kong, China, 12–14 December 2017; pp. 1–6.
17. Chen, X.; Wang, H.; Yi, H.; Wang, X.; Yan, X.; Guo, Z. Anthraquinone on Porous Carbon Nanotubes with Improved Supercapacitor Performance. *J. Phys. Chem. C* **2014**, *118*, 8262–8270. [CrossRef]
18. Salunkhe, R.R.; Tang, J.; Kamachi, Y.; Nakato, T.; Kim, J.H.; Yamauchi, Y. Asymmetric Supercapacitors Using 3D Nanoporous Carbon and Cobalt Oxide Electrodes Synthesized from a Single Metal–Organic Framework. *ACS Nano* **2015**, *9*, 6288–6296. [CrossRef] [PubMed]
19. Shen, L.; Wang, J.; Xu, G.; Li, H.; Dou, H.; Zhang, X. $NiCo_2S_4$ Nanosheets Grown on Nitrogen-Doped Carbon Foams as an Advanced Electrode for Supercapacitors. *Adv. Energy Mater.* **2014**, *5*, 1400977. [CrossRef]
20. Wang, K.; Wu, H.; Meng, Y.; Wei, Z. Conducting Polymer Nanowire Arrays for High Performance Supercapacitors. *Small* **2013**, *10*, 14–31. [CrossRef] [PubMed]

21. Xu, P.; Liu, J.; Yan, P.; Miao, C.; Ye, K.; Cheng, K.; Yin, J.; Cao, D.; Li, K.; Wang, G. Preparation of porous cadmium sulphide on nickel foam: A novel electrode material with excellent supercapacitor performance. *J. Mater. Chem. A* **2016**, *4*, 4920–4928. [CrossRef]

22. Durga, I.K.; Rao, S.S.; Reddy, A.E.; Gopi, C.V.V.M.; Kim, H.-J. Achieving copper sulfide leaf like nanostructure electrode for high performance supercapacitor and quantum-dot sensitized solar cells. *Appl. Surf. Sci.* **2018**, *435*, 666–675. [CrossRef]

23. Naresh, B.; Punnoose, D.; Rao, S.S.; Subramanian, A.; Ramesh, B.R.; Kim, H.-J. Hydrothermal synthesis and pseudocapacitive properties of morphology-tuned nickel sulfide (NiS) nanostructures. *New J. Chem.* **2018**, *42*, 2733–2742. [CrossRef]

24. Sekhar, S.C.; Nagaraju, G.; Cha, S.M.; Yu, J.S. Birnessite-type MnO_2 nanosheet arrays with interwoven arrangements on vapor grown carbon fibers as hybrid nanocomposites for pseudocapacitors. *Dalton Trans. Camb. Engl. 2003* **2016**, *45*, 19322–19328. [CrossRef] [PubMed]

25. Quan, W.; Jiang, C.; Wang, S.; Li, Y.; Zhang, Z.; Tang, Z.; Favier, F. New nanocomposite material as supercapacitor electrode prepared via restacking of Ni-Mn LDH and MnO_2 nanosheets. *Electrochim. Acta* **2017**, *247*, 1072–1079. [CrossRef]

26. Gao, Y.; Mi, L.; Wei, W.; Cui, S.; Zheng, Z.; Hou, H.; Chen, W. Double Metal Ions Synergistic Effect in Hierarchical Multiple Sulfide Microflowers for Enhanced Supercapacitor Performance. *ACS Appl. Mater. Interfaces* **2015**, *7*, 4311–4319. [CrossRef] [PubMed]

27. Enhancing the Supercapacitor Performance of Graphene/MnO2 Nanostructured Electrodes by Conductive Wrapping—Nano Letters (ACS Publications). Available online: https://pubs.acs.org/doi/10.1021/nl2026635 (accessed on 7 June 2018).

28. Zhou, W.; Zheng, J.-L.; Yue, Y.-H.; Guo, L. Highly stable rGO-wrapped Ni_3S_2 nanobowls: Structure fabrication and superior long-life electrochemical performance in LIBs. *Nano Energy* **2015**, *11*, 428–435. [CrossRef]

29. Fisher, R.A.; Watt, M.R.; Ready, W.J. Functionalized Carbon Nanotube Supercapacitor Electrodes: A Review on Pseudocapacitive Materials. *ECS J. Solid State Sci. Technol.* **2013**, *2*, M3170–M3177. [CrossRef]

30. Balamuralitharan, B.; Karthick, S.N.; Balasingam, S.K.; Hemalatha, K.V.; Selvam, S.; Raj, J.A.; Prabakar, K.; Jun, Y.; Kim, H.-J. Hybrid Reduced Graphene Oxide/Manganese Diselenide Cubes: A New Electrode Material for Supercapacitors. *Energy Technol.* **2017**, *5*, 1953–1962. [CrossRef]

31. Jiang, J.; Li, Y.; Liu, J.; Huang, X.; Yuan, C.; Lou, X.W.D. Recent advances in metal oxide-based electrode architecture design for electrochemical energy storage. *Adv. Mater.* **2012**, *24*, 5166–5180. [CrossRef] [PubMed]

32. Kim, H.J.; Kim, C.W.; Punnoose, D.; Gopi, C.V.; Kim, S.K.; Prabakar, K.; Rao, S.S. Nickel doped cobalt sulfide as a high performance counter electrode for dye-sensitized solar cells. *Appl. Surf. Sci.* **2015**, *328*, 78–85. [CrossRef]

33. Facile Preparation and Sulfidation Analysis for Activated Multiporous Carbon@NiCo2S4 Nanostructure with Enhanced Supercapacitive Properties. Available online: https://www.infona.pl/resource/bwmeta1.element.elsevier-0473b203-809f-3a8d-9472-94dfdf7cea64 (accessed on 7 June 2018).

34. Selvam, S.; Balamuralitharan, B.; Karthick, S.N.; Savariraj, A.D.; Hemalatha, K.V.; Kim, S.-K.; Kim, H.-J. Novel high-temperature supercapacitor combined dye sensitized solar cell from a sulfated β-cyclodextrin/PVP/$MnCO_3$ composite. *J. Mater. Chem. A* **2015**, *3*, 10225–10232. [CrossRef]

35. Ruthenium Sulfide Nanoparticles as a New Pseudocapacitive Material for Supercapacitor—ScienceDirect. Available online: https://www.sciencedirect.com/science/article/pii/S001346861632730X (accessed on 7 June 2018).

36. Zhang, C.; Higgins, T.M.; Park, S.-H.; O'Brien, S.E.; Long, D.; Coleman, J.N.; Nicolosi, V. Highly flexible and transparent solid-state supercapacitors based on RuO_2/PEDOT:PSS conductive ultrathin films. *Nano Energy* **2016**, *28*, 495–505. [CrossRef]

37. Karthik, P.; Vinoth, R.; Selvam, P.; Balaraman, E.; Navaneethan, M.; Hayakawa, Y.; Neppolian, B. A visible-light active catechol–metal oxide carbonaceous polymeric material for enhanced photocatalytic activity. *J. Mater. Chem. A* **2016**, *5*, 384–396. [CrossRef]

38. Bao, L.; Zang, J.; Li, X. Flexible Zn_2SnO_4/MnO_2 Core/Shell Nanocable−Carbon Microfiber Hybrid Composites for High-Performance Supercapacitor Electrodes. *Nano Lett.* **2011**, *11*, 1215–1220. [CrossRef] [PubMed]

39. Yu, M.; Sun, H.; Sun, X.; Lu, F.; Wang, G.; Hu, T.; Qiu, H.; Lian, J. Hierarchical Al-doped and Hydrogenated ZnO Nanowire@MnO$_2$ Ultra-Thin Nanosheet Core/Shell Arrays for High-Performance Supercapacitor Electrode. *Int. J. Electrochem. Sci.* **2013**, *8*, 17.

40. Xia, X.; Tu, J.; Zhang, Y.; Wang, X.; Gu, C.; Zhao, X.; Fan, H.J. High-Quality Metal Oxide Core/Shell Nanowire Arrays on Conductive Substrates for Electrochemical Energy Storage. *ACS Nano* **2012**, *6*, 5531–5538. [CrossRef] [PubMed]

41. Sun, X.; Li, Q.; Lü, Y.; Mao, Y. Three-dimensional ZnO@MnO$_2$ core@shell nanostructures for electrochemical energy storage. *Chem. Commun.* **2013**, *49*, 4456–4458. [CrossRef] [PubMed]

42. Yasir Rafiq, M.; Iqbal, F.; Aslam, F.; Bilal, M.; Munir, N.; Sultana, I.; Ashraf, F.; Manzoor, F.; Hassan, N.; Razaq, A. Fabrication and characterization of ZnO/MnO$_2$ and ZnO/TiO$_2$ flexible nanocomposites for energy storage applications. *J. Alloys Compd.* **2017**, *729*. [CrossRef]

43. Pearton, S.J.; Abernathy, C.R.; Overberg, M.E.; Thaler, G.T.; Norton, D.P.; Theodoropoulou, N.; Hebard, A.F.; Park, Y.D.; Ren, F.; Kim, J.; et al. Wide band gap ferromagnetic semiconductors and oxides. *J. Appl. Phys.* **2002**, *93*, 1–13. [CrossRef]

44. Ryu, Y.R.; Lubguban, J.A.; Lee, T.S.; White, H.W.; Jeong, T.S.; Youn, C.J.; Kim, B.J. Excitonic ultraviolet lasing in ZnO-based light emitting devices. *Appl. Phys. Lett.* **2007**, *90*, 131115. [CrossRef]

45. Xing, G.Z.; Lu, Y.H.; Tian, Y.F.; Yi, J.B.; Lim, C.C.; Li, Y.F.; Li, G.P.; Wang, D.D.; Yao, B.; Ding, J.; et al. Defect-induced magnetism in undoped wide band gap oxides: Zinc vacancies in ZnO as an example. *AIP Adv.* **2011**, *1*, 022152. [CrossRef]

46. Yan, D.; Liu, Y.; Li, Y.; Zhuo, R.; Wu, Z.G.; Ren, P.; Li, S.; Wang, J.; Yan, P.; Geng, Z. Synthesis and electrochemical properties of MnO$_2$/rGO/PEDOT:PSS ternary composite electrode material for supercapacitors. *Mater. Lett.* **2014**, *127*, 53–55. [CrossRef]

47. Ranjusha, R.; Sajesh, K.M.; Roshny, S.; Lakshmi, V.; Anjali, P.; Sonia, T.S.; Nair, A.S.; Subramanian, K.R.; Nair, S.V.; Chennazhi, K.P.; et al. Supercapacitors based on freeze dried MnO$_2$ embedded PEDOT: PSS hybrid sponges. *Microporous Mesoporous Mater.* **2014**, *186*, 30–36. [CrossRef]

48. Yin, C.; Yang, C.; Jiang, M.; Deng, C.; Yang, L.; Li, J.; Qian, D. A Novel and Facile One-Pot Solvothermal Synthesis of PEDOT–PSS/Ni–Mn–Co–O Hybrid as an Advanced Supercapacitor Electrode Material. *ACS Appl. Mater. Interfaces* **2016**, *8*, 2741–2752. [CrossRef] [PubMed]

49. Preparation and Electrochemical Performances of NiS with PEDOT: PSS Chrysanthemum Petal Like Nanostructure for High Performance Supercapacitors—ScienceDirect. Available online: https://www.sciencedirect.com/science/article/pii/S0013468617320054 (accessed on 7 June 2018).

50. Punnoose, D.; Rao, S.S.; Kim, H.-J. Solution processed metal-doped NiS/PEDOT:PSS composite thin films as an efficient electrode for quantum-dot sensitized solar cells. *Mater. Res. Bull.* **2018**, *102*, 369–378. [CrossRef]

51. Krishnakumar, S.R.; Shanthi, N.; Sarma, D.D. Electronic structure of millerite NiS. *Phys. Rev. B* **2002**, *66*, 115105. [CrossRef]

52. Gao, R.; Zhang, Q.; Soyekwo, F.; Lin, C.; Lv, R.; Qu, Y.; Chen, M.; Zhu, A.; Liu, Q. Novel amorphous nickel sulfide@CoS double-shelled polyhedral nanocages for supercapacitor electrode materials with superior electrochemical properties. *Electrochim. Acta* **2017**, *237*, 94–101. [CrossRef]

53. Krishnamoorthy, K.; Kumar, G.; Radhakrishnan, S.; Jae Kim, S. One pot hydrothermal growth of hierarchical nanostructured Ni$_3$S$_2$ on Ni foam for supercapacitor application. *Chem. Eng. J.* **2014**, *251*, 116–122. [CrossRef]

54. Zhang, Y.; Sun, W.; Rui, X.; Li, B.; Tan, H.T.; Guo, G.; Madhavi, S.; Zong, Y.; Yan, Q. One-Pot Synthesis of Tunable Crystalline Ni3S4@Amorphous MoS$_2$ Core/Shell Nanospheres for High-Performance Supercapacitors. *Small* **2015**, *11*, 3694–3702. [CrossRef] [PubMed]

55. Punnoose, D.; Kumar, C.S.S.P.; Rao, S.S.; Varma, C.V.T.; Naresh, B.; Reddy, A.E.; Kundarala, N.; Lee, Y.-S.; Kim, M.-Y.; Kim, H.-J. In situ synthesis of CuS nano platelets on nano wall networks of Ni foam and its application as an efficient counter electrode for quantum dot sensitized solar cells. *Org. Electron.* **2017**, *42*, 115–122. [CrossRef]

56. Rao, S.S.; Durga, I.K.; Kundakarla, N.; Punnoose, D.; Gopi, C.V.; Reddy, A.E.; Jagadeesh, M.; Kim, H.J. A hydrothermal reaction combined with a post anion-exchange reaction of hierarchically nanostructured NiCo$_2$S$_4$ for high-performance QDSSCs and supercapacitors. *New J. Chem.* **2017**, *41*, 10037–10047. [CrossRef]

57. Kim, J.Y.; Jung, J.H.; Lee, D.E.; Joo, J. Enhancement of electrical conductivity of poly(3,4-ethylenedioxythiophene)/poly(4-styrenesulfonate) by a change of solvents. *Synth. Met.* **2002**, *126*, 311–316. [CrossRef]

58. Tian, J.; Lin, B.; Sun, Y.; Zhang, X.; Yang, H. Porous WO$_3$@CuO composites derived from polyoxometalates@metal organic frameworks for supercapacitor. *Mater. Lett.* **2017**, *206*, 91–94. [CrossRef]

59. Ramesh, S.; Haldorai, Y.; Sivasamy, A.; Kim, H.S. Nanostructured Co$_3$O$_4$/nitrogen doped carbon nanotube composites for high-performance supercapacitors. *Mater. Lett.* **2017**, *206*, 39–43. [CrossRef]

60. Lee, K.S.; Park, C.W.; Kim, J.D. Synthesis of ZnO/Activated Carbon with High Surface Area for Supercapacitor Electrodes. 2018. Available online: https://www.sciencedirect.com/science/article/pii/S0927775718305946 (accessed on 28 June 2018).

61. Sasirekha, C.; Arumugam, S.; Muralidharan, G. Green synthesis of ZnO/carbon (ZnO/C) as an electrode material for symmetric supercapacitor devices. *Appl. Surf. Sci.* **2018**, *449*, 521–527. [CrossRef]

62. Saranya, M.; Ramachandran, R.; Wang, F. Graphene-zinc oxide (G-ZnO) nanocomposite for electrochemical supercapacitor applications. *J. Sci. Adv. Mater. Dev.* **2016**, *1*, 454–460. [CrossRef]